The Astrophysical Journal, 912:101 (13pp), 2021 May 10 https://doi.org/10.3847/1538-4357/abed51

Dependence of Solar Wind Proton Temperature on the Polarization Properties of Alfvénic Fluctuations at Ion-kinetic Scales

L. D. Woodham[1], R. T. Wicks[2,3,4], D. Verscharen[3,5], J. M. TenBarge[6,7], and G. G. Howes[8]
[1] Department of Physics, The Blackett Laboratory, Imperial College London, London, SW7 2AZ, UK; l.woodham@imperial.ac.uk
[2] Department of Mathematics, Physics & Electrical Engineering, Northumbria University, Newcastle upon Tyne, NE1 8ST, UK
[3] Mullard Space Science Laboratory, University College London, Holmbury St. Mary, Surrey RH5 6NT, UK
[4] Institute of Risk and Disaster Reduction, University College London, London, WC1E 6BT, UK
[5] Space Science Center, University of New Hampshire, Durham, NH 03824, USA
[6] Department of Astrophysical Sciences, Princeton University, Princeton, NJ 08544, USA
[7] Princeton Plasma Physics Laboratory, Princeton, NJ 08540, USA
[8] Department of Physics and Astronomy, University of Iowa, Iowa City, IA 52242, USA
Received 2021 January 27; revised 2021 March 8; accepted 2021 March 8; published 2021 May 10

Abstract

We use fluctuating magnetic helicity to investigate the polarization properties of Alfvénic fluctuations at ion-kinetic scales in the solar wind as a function of β_p, the ratio of proton thermal pressure to magnetic pressure, and θ_{vB}, the angle between the proton flow and local mean magnetic field, $\boldsymbol{B}_0$. Using almost 15 yr of Wind observations, we separate the contributions to helicity from fluctuations with wavevectors, $\boldsymbol{k}$, quasi-parallel and oblique to $\boldsymbol{B}_0$, finding that the helicity of Alfvénic fluctuations is consistent with predictions from linear Vlasov theory. This result suggests that the nonlinear turbulent fluctuations at these scales share at least some polarization properties with Alfvén waves. We also investigate the dependence of proton temperature in the β_p–θ_{vB} plane to probe for possible signatures of turbulent dissipation, finding that it correlates with θ_{vB}. The proton temperature parallel to $\boldsymbol{B}_0$ is higher in the parameter space where we measure the helicity of right-handed Alfvénic fluctuations, and the temperature perpendicular to $\boldsymbol{B}_0$ is higher where we measure left-handed fluctuations. This finding is inconsistent with the general assumption that by sampling different θ_{vB} in the solar wind we can analyze the dependence of the turbulence distribution on θ_{kB}, the angle between $\boldsymbol{k}$ and $\boldsymbol{B}_0$. After ruling out both instrumental and expansion effects, we conclude that our results provide new evidence for the importance of local kinetic processes that depend on θ_{vB} in determining proton temperature in the solar wind.

Unified Astronomy Thesaurus concepts: Heliosphere (711); Solar wind (1534); Space plasmas (1544); Plasma physics (2089); Interplanetary turbulence (830); Alfven waves (23); Magnetic fields (994); The Sun (1693)

1. Introduction

The solar wind is a variable flow of plasma that escapes from the solar corona out into the heliosphere. In situ measurements of the solar wind provide insights into the fundamental physical processes occurring in expanding astrophysical plasmas. Fluctuations in the solar wind plasma and electromagnetic fields exist over many orders of magnitude in scale, linking both microscopic and macroscopic processes (see Matteini et al. 2012; Alexandrova et al. 2013, and references therein). The couplings between large-scale dynamics and small-scale kinetic processes are central to our understanding of energy transport and heating in these plasmas (Verscharen et al. 2019). There are still many open questions with regard to wave dissipation and plasma heating in collisionless plasmas. Understanding these mechanisms in the collisionless solar wind plasma is a major outstanding problem in the field of heliophysics research.

In solar wind originating from open field lines in the corona, fluctuations are predominantly Alfvénic (Coleman 1968; Belcher et al. 1969; Belcher & Davis 1971), with only a small compressional component (Howes et al. 2012; Klein et al. 2012; Chen 2016; Šafránková et al. 2019). At scales 10^5 m $\lesssim L \lesssim 10^8$ m, called the inertial range, nonlinear interactions between fluctuations lead to a turbulent cascade of energy toward smaller scales (Tu & Marsch 1995; Bruno & Carbone 2013). This range is characterized by fluctuations with increasing anisotropy toward smaller scales, $k_\perp \gg k_\parallel$, where $k_\parallel$ and $k_\perp$ are components of the wavevector, $\boldsymbol{k}$, in the direction parallel and perpendicular to the local mean magnetic field, $\boldsymbol{B}_0$, respectively (Horbury et al. 2008; MacBride et al. 2010; Wicks et al. 2010; Chen et al. 2011, 2012). At scales close to the proton inertial length, d_p, and proton gyroradius, ρ_p, typically $L \sim 10^5$ m at 1 au, the properties of the fluctuations change owing to Hall (Galtier 2006; Galtier & Buchlin 2007) and finite-Larmor-radius (Howes et al. 2006; Schekochihin et al. 2009; Boldyrev & Perez 2012) effects. The nonlinear turbulent fluctuations at these ion-kinetic scales exhibit some properties that are consistent with those of kinetic Alfvén waves (KAWs; Leamon et al. 1999; Bale et al. 2005; Howes et al. 2008; Sahraoui et al. 2010; Woodham et al. 2019).

Solar wind proton velocity distribution functions (VDFs) typically deviate from local thermal equilibrium owing to a low rate of collisional relaxation (Kasper et al. 2008, 2017; Marsch 2012; Maruca et al. 2013). The coupling of small-scale electromagnetic fluctuations and the kinetic features of the proton VDFs can lead to energy transfer between fluctuating fields and the particles. Collisionless damping of these fluctuations can lead to dissipation of turbulence via wave–particle interactions such as Landau (Leamon et al. 1999; Howes et al. 2008) and cyclotron (Marsch et al. 1982, 2003; Isenberg & Vasquez 2019) resonance, or other processes such as stochastic heating (Chandran et al. 2010, 2013) and reconnection-based mechanisms (Sundkvist et al. 2007; Perri et al. 2012). These mechanisms are dependent on the modes present and the background plasma conditions, i.e., a function

of the ratio of proton thermal pressure to magnetic pressure, $\beta_p = n_p k_B T_p / (B_0^2 / 2\mu_0)$, where n_p is the proton density and T_p is the proton temperature. Each mechanism leads to distinct fine structure in proton VDFs, increasing the effective collision rate. These processes ultimately lead to plasma heating and therefore changes in the macroscopic properties of the plasma (e.g., Marsch 2006).

In addition to damping of turbulent fluctuations, non-Maxwellian features of solar wind VDFs such as temperature anisotropies relative to $\boldsymbol{B}_0$, beam populations, and relative drifts between plasma species provide sources of free energy for instabilities at ion-kinetic scales (Kasper et al. 2002b, 2008, 2013; Hellinger et al. 2006; Bale et al. 2009; Maruca et al. 2012; Bourouaine et al. 2013; Gary et al. 2015; Alterman et al. 2018). These modes grow until the free energy source is removed, acting to limit departure from an isotropic Maxwellian. Ion-scale kinetic instabilities are prevalent in collisionally young solar wind (Klein et al. 2018, 2019), although the interaction between instabilities and the background turbulence is still poorly understood (e.g., Klein & Howes 2015). As the solar wind flows out into the heliosphere, instabilities, local heating, heat flux, and collisions all alter the macroscopic thermodynamics of the plasma through coupling between small-scale local processes and large-scale dynamics. These processes lead to a deviation from Chew–Goldberger–Low theory (CGL; Chew et al. 1956) for double adiabatic expansion (Matteini et al. 2007).

Alfvénic fluctuations in the solar wind are characterized by magnetic field fluctuations, $\delta\boldsymbol{B}$, with a quasi-constant field magnitude, $|\boldsymbol{B}|$. Since the fluctuations have large amplitudes, $\delta\boldsymbol{B}/\boldsymbol{B}_0 \sim 1$, the magnetic field vector traces out a sphere of constant radius (Barnes 1981), leading to fluctuations in the angle, θ_{RB}, between the local field, $\boldsymbol{B} = \boldsymbol{B}_0 + \delta\boldsymbol{B}$, and the radial direction. These fluctuations correlate with proton motion, and therefore the solar wind bulk velocity, $\boldsymbol{v}_{\rm sw}$, also exhibits a dependence on θ_{RB} (Matteini et al. 2014, 2015). If these fluctuations play a role in plasma heating, we also expect a correlation between them and the proton temperature. Recent studies have shown that the proton temperature anisotropy at 1 au exhibits a dependence on θ_{RB} (D'Amicis et al. 2019a) that is not present closer to the Sun (Horbury et al. 2018), suggesting ongoing dynamical processes related to these fluctuations in the solar wind. In fact, larger wave power in transverse Alfvénic fluctuations is also correlated with proton temperature anisotropy (Bourouaine et al. 2010), consistent with an increase in fluctuations in θ_{RB}.

Single-spacecraft observations have an inherent spatiotemporal ambiguity that complicates investigation of the coupling between Alfvénic fluctuations and the plasma bulk parameters. These measurements are restricted to the sampling of a time series defined by the trajectory of the spacecraft with respect to the flow velocity, $\boldsymbol{v}_{\rm sw}$. This limitation means that we can only resolve the component of $\boldsymbol{k}$ along the sampling direction, i.e., predominantly the radial direction. Previous studies (e.g., Horbury et al. 2008; Wicks et al. 2010; He et al. 2011; Podesta & Gary 2011a) assume that the underlying distribution of turbulence in the solar wind is independent of θ_{vB}, the angle between $\boldsymbol{v}_{\rm sw}$ and $\boldsymbol{B}_0$. Based on this assumption, these studies use measurements of the solar wind plasma at different θ_{vB} to probe the turbulence as a function of θ_{kB}, the angle between $\boldsymbol{k}$ and $\boldsymbol{B}_0$. However, if there is indeed a dependence of the plasma bulk parameters (including the temperature and temperature anisotropies as observed) on $\theta_{RB} \simeq \theta_{vB}$, then this assumption may not be valid.

In this paper, we investigate whether the solar wind proton temperature anisotropy depends on the polarization properties of small-scale Alfvénic fluctuations, and hence θ_{vB}, in the context of turbulent dissipation. In Section 2, we discuss the linear theory and polarization properties of Alfvén waves. In Sections 3 and 4, we describe our analysis methods, using single-spacecraft measurements to measure the polarization properties of Alfvénic fluctuations at ion-kinetic scales in the solar wind. We present our main results in Section 5, testing how the dissipation of turbulence at these scales affects the macroscopic bulk properties of the solar wind. We show that Alfvénic fluctuations present at ion-kinetic scales in the solar wind share at least some polarization properties with Alfvén waves from linear Vlasov theory. By also investigating the statistical distribution of proton temperature in the β_p–θ_{vB} plane, we find that there is a clear dependence in this reduced parameter space that also correlates with the magnetic helicity of Alfvénic fluctuations. We discuss the implications of our results in Section 6, namely, that we cannot sample different θ_{vB} to analyze the dependence of the turbulence on θ_{kB} without considering other plasma properties. In Section 7, we consider both instrumental and expansion effects, showing that they do not account for the observed temperature distribution. Finally, in Section 8, we conclude that our results provide new evidence for the importance of local kinetic processes that depend on θ_{vB} in determining proton temperature in the solar wind.

2. Polarization Properties of Alfvén Waves

In collisionless space plasmas such as the solar wind, the linearized Vlasov equation describes linear waves and instabilities. Nontrivial solutions exist only when the complex frequency, $\omega = \omega_r + i\gamma$, solves the hot-plasma dispersion relation (Stix 1992). Here ω_r is the wave frequency and γ is the wave growth ($\gamma > 0$) or damping ($\gamma < 0$) rate. One such solution is the Alfvén wave, which is ubiquitous in space plasmas. At $k_\parallel d_p \ll 1$ and $k_\perp \rho_p \ll 1$, this wave is incompressible and propagates along $\boldsymbol{B}_0$ at the Alfvén speed, $v_{\rm A}$, resulting in transverse perturbations to the field (Alfvén 1942). The fluctuations in velocity, $\delta\boldsymbol{v}$, and the magnetic field, $\delta\boldsymbol{b}$, exhibit a characteristic (anti)correlation, $\delta\boldsymbol{v} = \mp\delta\boldsymbol{b}$, for propagation (parallel) antiparallel to $\boldsymbol{B}_0$. Here $\boldsymbol{b}$ is the magnetic field in Alfvén units, $\boldsymbol{b} = \boldsymbol{B}/\sqrt{\mu_0 \rho}$, where ρ is the plasma mass density. The Alfvén wave has the dispersion relation

$$\omega_r(k) = k v_{\rm A} \cos\theta_{kB}. \tag{1}$$

Approaching ion-kinetic scales, $k_\parallel d_p \simeq 1$ or $k_\perp \rho_p \simeq 1$, the dispersion relation splits into two branches: the Alfvén ion cyclotron (AIC) wave for small θ_{kB} (Gary & Borovsky 2004), and the KAW for large θ_{kB} (Gary & Nishimura 2004).

We define the polarization of a wave as

$$P = -\frac{i\delta E_y}{\delta E_x}\frac{\omega_r}{|\omega_r|}, \tag{2}$$

where δE_x and δE_y are components of the Fourier amplitudes of the fluctuating electric field transverse to $\boldsymbol{B}_0 = B_0\,\hat{\boldsymbol{z}}$ (Stix 1992; Gary 1993). Therefore, P gives the sense and degree of rotation in time of a fluctuating electric field vector at a fixed point in space, viewed in the direction parallel to $\boldsymbol{B}_0$. A circularly polarized wave has $P = \pm 1$, where $+1$ (-1) designates right-

handed (left-handed) polarization. In this definition, a right-hand-polarized wave has electric field vectors that rotate in the same sense as the gyration of an electron; a left-hand-polarized wave, the same sense as ions. For more general elliptical polarization, we take the real part, Re(P).

Magnetic helicity is a measure of the degree and sense of spatial rotation of the magnetic field (Woltjer 1958a, 1958b). It is an invariant of ideal magnetohydrodynamics (MHD) and defined as a volume integral over all space:

$$H_m \equiv \int_V \boldsymbol{A} \cdot \boldsymbol{B}\, d^3\boldsymbol{r}, \tag{3}$$

where $\boldsymbol{A}$ is the magnetic vector potential defined by $\boldsymbol{B} = \nabla \times \boldsymbol{A}$. Matthaeus et al. (1982) propose the fluctuating magnetic helicity, $H_m'(\boldsymbol{k})$, as a diagnostic of solar wind fluctuations, which in spectral form (i.e., in Fourier space) is defined as

$$H_m'(\boldsymbol{k}) \equiv \delta\boldsymbol{A}(\boldsymbol{k}) \cdot \delta\boldsymbol{B}^*(\boldsymbol{k}), \tag{4}$$

where $\delta\boldsymbol{A}$ is the fluctuating vector potential and the asterisk indicates the complex conjugate of the Fourier coefficients (Matthaeus & Goldstein 1982b). This definition removes contributions to the helicity arising from $\boldsymbol{B}_0$. By assuming the Coulomb gauge, $\nabla \cdot \boldsymbol{A} = 0$, the fluctuating magnetic helicity can be written as

$$H_m{}'(\boldsymbol{k}) = i\frac{\delta B_y \delta B_z^* - \delta B_y^* \delta B_z}{k_x}, \tag{5}$$

where the components of $\delta\boldsymbol{B}(\boldsymbol{k})$ are Fourier coefficients of a wave mode with $\boldsymbol{k}$. This result is invariant under cyclic permutations of the three components x, y, z (see Equation (2) in Howes & Quataert 2010). We define the normalized fluctuating magnetic helicity density as

$$\sigma_m(\boldsymbol{k}) \equiv \frac{kH_m'(\boldsymbol{k})}{|\delta\boldsymbol{B}(\boldsymbol{k})|^2}, \tag{6}$$

where $|\delta\boldsymbol{B}(\boldsymbol{k})|^2 = \delta B_x^* \delta B_x + \delta B_y^* \delta B_y + \delta B_z^* \delta B_z$. Here $\sigma_m(\boldsymbol{k})$ is dimensionless and takes values in the interval $[-1, 1]$, where $\sigma_m = -1$ indicates fluctuations with purely left-handed helicity and $\sigma_m = +1$ purely right-handed helicity. A value of $\sigma_m = 0$ indicates no overall coherence, i.e., there are either no fluctuations with coherent handedness or there is equal power in both left-handed and right-handed components so that the net value is zero.

Gary (1986) first explored the dependence of Re(P) for small-scale Alfvén waves on different parameters by numerically solving the full electromagnetic dispersion relation, showing that it changes sign depending on both θ_{kB} and β_p. In the cold-plasma limit ($\beta_p \ll 1$), the Alfvén wave has Re(P) < 0 for all θ_{kB}. However, from linear Vlasov theory, at $\beta_p \simeq 10^{-2}$, the wave has Re(P) < 0 for $0^\circ \leqslant \theta_{kB} \lesssim 80^\circ$ but has Re(P) > 0 for $\theta_{kB} \gtrsim 80^\circ$. As β_p increases, the wave has Re(P) > 0 for an increasing range of oblique angles so that at $\beta_p \simeq 10$ the transition occurs at about 40°. This result reveals that the changing polarization properties on both θ_{kB} and β_p will affect possible wave–particle interactions and hence turbulence damping mechanisms that can occur in a plasma. For example, left-handed AIC waves can cyclotron resonate with ions, leading to heating perpendicular to $\boldsymbol{B}_0$. On the other hand, right-handed KAWs are compressive at small scales, giving rise to density fluctuations and a nonzero component of the wave electric field, $E_\parallel \neq 0$. Hence, KAWs can Landau-resonate with both electrons and ions, leading to heating parallel to $\boldsymbol{B}_0$.

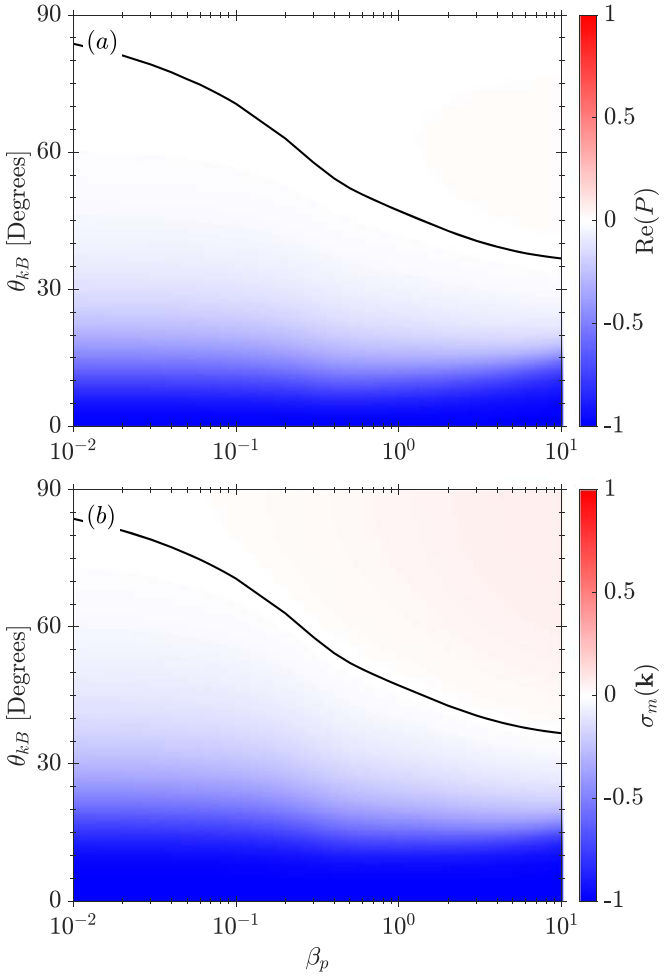

Figure 1. (a) Real part of the polarization, Re(P), and (b) normalized fluctuating magnetic helicity density, $\sigma_m(\boldsymbol{k})$, of Alfvén waves with $kd_p = 0.05$ as a function of β_p and θ_{kB}, calculated using the NHDS code (see main text). The black lines indicate the isocontours Re(P) $= 0$ and $\sigma_m(\boldsymbol{k}) = 0$.

We plot both Re(P) and $\sigma_m(\boldsymbol{k})$ for Alfvénic fluctuations across the β_p–θ_{kB} plane in Figure 1. The black lines are isocontours of Re(P) $= 0$ and $\sigma_m(\boldsymbol{k}) = 0$, respectively. We note that for waves with $\theta_{kB} \simeq 0^\circ$ there is no difference between the values of Re(P) and $\sigma_m(\boldsymbol{k})$. To calculate these lines, we solve the linear Vlasov equation using the New Hampshire Dispersion relation Solver (NHDS; Verscharen et al. 2013; Verscharen & Chandran 2018). Here $\boldsymbol{k} = k_\perp \hat{\boldsymbol{x}} + k_\parallel \hat{\boldsymbol{z}}$, and we assume a plasma consisting of protons and electrons with isotropic Maxwellian distributions, equal density and temperature, and no drifting components. We set $kd_p = 0.05$,[9] where the angle θ_{kB} defines $k_\perp = k \sin\theta_{kB}$ and $k_\parallel = k \cos\theta_{kB}$. Therefore, $k_\parallel d_p$ and $k_\perp \rho_p$ change throughout the β_p–θ_{kB} plane,[10] while the normalized scale of the waves remains constant. We also set $v_A/c = 10^{-4}$, which is typical for solar wind conditions where $v_A \simeq 50$ km s^{-1} (Klein et al. 2019). While our assumption of an isotropic proton–electron plasma is not truly representative of

[9] The black lines in Figure 1 are constant over the range $kd_p = [0.01, 1]$.
[10] The scales d_p and ρ_p are related by $\rho_p = d_p\sqrt{\beta_p}$.

the more complex ion VDFs typically observed in the solar wind, protons remain the most important ion component for solar wind interaction with Alfvénic fluctuations. Therefore, we expect that the polarization properties of Alfvénic fluctuations in the solar wind are adequately described by the theoretical description provided in Figure 1.

3. Reduced Spectra from Spacecraft Measurements

In the solar wind, the polarization properties of fluctuations are typically determined using the fluctuating magnetic helicity. However, from a single-spacecraft time series of magnetic field measurements, it is only possible to determine a reduced form of the helicity (Batchelor 1970; Montgomery & Turner 1981; Matthaeus et al. 1982):

$$H'^{r}_{m}(\omega_{sc}) = \frac{2\,\mathrm{Im}\,\{\mathcal{P}^{r}_{TN}(\omega_{sc})\}}{k_r}, \tag{7}$$

where ω_{sc} is the frequency of the fluctuations in the spacecraft frame, $k_r = k\cos\theta_{kv}$ is the component of the wavevector along the flow direction of the solar wind plasma, $\boldsymbol{v}_{sw}$, and θ_{kv} is the angle between $\boldsymbol{k}$ and $\boldsymbol{v}_{sw}$. Here

$$\mathcal{P}^{r}_{ij}(\omega_{sc}) = \delta B^{*}_{i}(\omega_{sc})\cdot\delta B_{j}(\omega_{sc}) \tag{8}$$

is the reduced power spectral tensor, where the $\delta B_i(\omega_{sc})$ are the complex Fourier coefficients of the time series of $\boldsymbol{B}$ in radial-tangential-normal (RTN) coordinates.[11] In this coordinate system, the solar wind flow is approximately radial, $\boldsymbol{v}_{sw} \simeq v_{sw}\,\hat{\boldsymbol{R}}$. The reduced tensor is an integral of the true spectral tensor, $\mathcal{P}_{ij}(\boldsymbol{k})$ (Fredricks & Coroniti 1976; Forman et al. 2011; Wicks et al. 2012):

$$\mathcal{P}^{r}_{ij}(\omega_{sc}) = \int \mathcal{P}_{ij}(\boldsymbol{k})\,\delta[\omega_{sc} - (\boldsymbol{k}\cdot\boldsymbol{v}_{sw} + \omega_{pl})]\,d^{3}\boldsymbol{k}. \tag{9}$$

Taylor's hypothesis (Taylor 1938) assumes that the fluctuations in the solar wind evolve slowly as they are advected past the spacecraft so that the plasma-frame frequency, ω_{pl}, satisfies $|\omega_{pl}| \ll |\boldsymbol{k}\cdot\boldsymbol{v}_{sw}|$ (Matthaeus & Goldstein 1982b; Perri & Balogh 2010). Therefore, the Doppler shift of the fluctuations into the spacecraft frame becomes

$$\omega_{sc} = \omega_{pl} + \boldsymbol{k}\cdot\boldsymbol{v}_{sw} \simeq \boldsymbol{k}\cdot\boldsymbol{v}_{sw} \equiv k_r v_{sw}, \tag{10}$$

so that the ω_{pl} term drops from Equation (9). Then, a time series of magnetic field measurements under these assumptions represents a spatial cut through the plasma, and we can write $\mathcal{P}^{r}_{ij}$ and H'^{r}_{m} as functions of k_r using Equation (10). However, it is not possible to determine the full wavevector, $\boldsymbol{k}$, or θ_{kB}, from single-spacecraft measurements. Since $v_A \ll v_{sw}$, Taylor's hypothesis is usually well satisfied for Alfvén waves in the solar wind with the dispersion relation given by Equation (1), as well as for the small-wavelength extensions of the Alfvén branch under the parameters considered here (see Howes et al. 2014; Klein et al. 2014a).

[11] In the RTN coordinate system, $\hat{\boldsymbol{R}}$ is the unit vector from the Sun toward the spacecraft, $\hat{\boldsymbol{T}}$ is the cross-product of the solar rotation axis and $\hat{\boldsymbol{R}}$, and $\hat{\boldsymbol{N}}$ completes the right-handed triad.

Based on the definition in Equation (6), the normalized reduced fluctuating magnetic helicity density is then defined as

$$\sigma^{r}_{m}(k_r) \equiv \frac{k_r H'^{r}_{m}(k_r)}{|\delta\boldsymbol{B}(k_r)|^2} = \frac{2\,\mathrm{Im}\,\{\mathcal{P}^{r}_{TN}(k_r)\}}{\mathrm{Tr}\,\{\mathcal{P}^{r}(k_r)\}}, \tag{11}$$

where Tr{} denotes the trace. Previous studies (e.g., Horbury et al. 2008; Wicks et al. 2010; He et al. 2011; Podesta & Gary 2011a) use θ_{vB} as a measure of a specific θ_{kB} in the solar wind. For example, measurements of $\sigma^{r}_{m}(k_r)$ separated as a function of θ_{vB} show a broad right-handed signature at oblique angles and a narrow left-handed signature at quasi-parallel angles (He et al. 2011, 2012a, 2012b; Podesta & Gary 2011a; Klein et al. 2014b; Bruno & Telloni 2015; Telloni et al. 2015). These signatures are associated with KAW-like fluctuations from the turbulent cascade and ion-kinetic instabilities, respectively (Telloni & Bruno 2016; Woodham et al. 2019).

By defining the field-aligned coordinate system,

$$\hat{\boldsymbol{z}} = \frac{\boldsymbol{B}_0}{|\boldsymbol{B}_0|};\ \hat{\boldsymbol{y}} = -\frac{\boldsymbol{v}_{sw}\times\boldsymbol{B}_0}{|\boldsymbol{v}_{sw}\times\boldsymbol{B}_0|};\ \hat{\boldsymbol{x}} = \hat{\boldsymbol{y}}\times\hat{\boldsymbol{z}}, \tag{12}$$

so that $\boldsymbol{v}_{sw}$ lies in the x–z plane with angle θ_{vB} from the $\hat{\boldsymbol{z}}$ direction (Wicks et al. 2012; Woodham et al. 2019), we can decompose $\sigma^{r}_{m}(k_r)$ into the components

$$\sigma_{ij}(k_l) = \frac{2\,\mathrm{Im}\,\{\mathcal{P}^{r}_{ij}(k_l)\}}{\mathrm{Tr}\,\{\mathcal{P}^{r}(k_l)\}}, \tag{13}$$

where the indices i, j, $l = x$, y, z. We derive the following relationship between the components $\sigma_{ij}(k_l)$ and $\sigma^{r}_{m}(k_r)$ (see the Appendix):

$$\sigma_{xy}(k_z) = \sigma^{r}_{m}(k_r)\frac{k_z}{k_r}, \tag{14}$$

$$\sigma_{xz}(k_y) = -\sigma^{r}_{m}(k_r)\frac{k_y}{k_r}, \tag{15}$$

and

$$\sigma_{yz}(k_x) = \sigma^{r}_{m}(k_r)\frac{k_x}{k_r}. \tag{16}$$

For fluctuations with $k_z \gg k_x$, i.e., $\boldsymbol{k}$ quasi-parallel to $\boldsymbol{B}_0$, $\sigma_{xy}(k_z)$ is the dominant contribution to $\sigma^{r}_{m}(k_r)$. Similarly, $\sigma_{yz}(k_x)$ dominates for modes with $k_x \gg k_z$, i.e., $\boldsymbol{k}$ at oblique angles, $\theta_{kB} \gtrsim 60°$. As the solar wind velocity is confined to the x–z plane, we have no information about k_y from single-spacecraft measurements, and $\sigma_{xz}(k_y)$ is not useful in a practical sense. From Section 2, we expect that AIC waves generated by kinetic instabilities have $k_z \gg k_x$. The anisotropic Alfvénic turbulent cascade leads to the generation of nearly perpendicular wavevectors with $k_x \gg k_z$. Therefore, we can separate the helicity signatures of the two kinetic scale branches of the Alfvén wave using our decomposition technique.

4. Data Analysis

We analyze magnetic field data from the Magnetic Field Investigation (MFI) fluxgate magnetometer (Lepping et al. 1995; Koval & Szabo 2013) and proton data from the SWE Faraday cup (Ogilvie et al. 1995; Kasper et al. 2006) instruments on board the Wind spacecraft from 2004 June to 2018 October. For each proton measurement, we define a local mean field, $\boldsymbol{B}_0$, averaged over the Solar Wind Experiment

(SWE) integration time (∼92 s). We estimate the normalized cross-helicity (Matthaeus & Goldstein 1982a) for each ∼92 s interval,

$$\sigma_c = \frac{2(\delta \boldsymbol{v} \cdot \delta \boldsymbol{b})}{|\delta \boldsymbol{v}|^2 + |\delta \boldsymbol{b}|^2}, \tag{17}$$

where $\delta \boldsymbol{b} = \boldsymbol{b} - \langle \boldsymbol{b} \rangle_{1\ \mathrm{hr}}$ and $\delta \boldsymbol{v} = \boldsymbol{v}_{\mathrm{sw}} - \langle \boldsymbol{v}_{\mathrm{sw}} \rangle_{1\ \mathrm{hr}}$. Here the mean is over a 1 hr window centered on the instantaneous values, and we assume that $\boldsymbol{v}_{\mathrm{sw}} \simeq \boldsymbol{v}_p$, where $\boldsymbol{v}_p$ is the proton bulk velocity. An averaging interval of 1 hr gives σ_c for fluctuations in the inertial range. The cross-helicity, $\sigma_c \in [-1, 1]$, is a measure of the (anti)correlation between velocity and magnetic field fluctuations, and therefore Alfvénicity (e.g., D'Amicis & Bruno 2015; D'Amicis et al. 2019b; Stansby et al. 2019; Perrone et al. 2020). A value $|\sigma_c| = 1$ indicates purely unbalanced Alfvénic fluctuations propagating in one direction, whereas $\sigma_c = 0$ indicates either balanced (equal power in opposite directions) or a lack of Alfvénic fluctuations. In the case of $\sigma_c = 0$, we expect no coherent value of $|\sigma_m| > 0$ at ion-kinetic scales.

Similarly to Woodham et al. (2019), we account for heliospheric sector structure in the magnetic field measurements by calculating σ_c averaged over a running window of 12 hr. For solar wind fluctuations dominantly propagating antisunward, the sign of σ_c depends only on the direction of $\boldsymbol{B}_0$. Therefore, if $\langle \sigma_c \rangle > 0$, we reverse the signs of the B_R and B_T components for each ∼92 s measurement so that sunward fields are rotated antisunward. This procedure removes the inversion of the sign of magnetic helicity due to the direction of the large-scale magnetic field with respect to the Sun.[12] We transform the 11 Hz magnetic field data associated with each proton measurement into field-aligned coordinates (Equation (12)) using $\boldsymbol{B}_0$ averaged over ∼92 s. We then compute the continuous wavelet transform (Torrence & Compo 1998) using a Morlet wavelet to calculate the magnetic helicity spectra, σ_{xy} and σ_{yz}, as functions of $f_{\mathrm{sc}} = \omega_{\mathrm{sc}}/2\pi$ using Equation (13). We average the spectra over ∼92 s, corresponding to the SWE measurement cadence, to ensure that the fluctuations contributing to the helicity spectra persist for at least several proton gyroperiods, $2\pi/\Omega_p$, giving a clear coherent helicity signature at ion-kinetic scales.

We estimate the amplitudes of σ_{xy} and σ_{yz} at ion-kinetic scales by fitting a Gaussian function to the coherent peak in each spectrum at frequencies close to the Taylor-shifted frequencies, v_{sw}/d_p and v_{sw}/ρ_p (see Woodham et al. 2018). We neglect any peak at $f > f_{\mathrm{noise}}$, where f_{noise} is the frequency above which instrumental noise of the MFI magnetometer becomes significant.[13] We also reject a spectrum if the angular deviation in $\boldsymbol{B}$ exceeds 15° during the ∼92 s measurement period to ensure that we measure the anisotropy of fluctuations at ion-kinetic scales with sufficient accuracy (see also Section 7.1). We designate the amplitude of the peak in each σ_{xy} spectrum as $\sigma_\parallel \equiv \max_{k_z} \sigma_{xy}(k_z)$ to diagnose the helicity of the modes with $\boldsymbol{k}$ quasi-parallel to $\boldsymbol{B}_0$, and σ_{yz} as $\sigma_\perp \equiv \max_{k_x} \sigma_{yz}(k_x)$ to diagnose the helicity of the modes with $\boldsymbol{k}$ oblique to $\boldsymbol{B}_0$ (see Section 3 and the Appendix).

In our analysis, we include only measurements of Alfvénic solar wind, $|\sigma_c| \geqslant 0.8$, and low collisionality, $N_c < 1$, which contain the strongest Alfvénic fluctuations with a nonzero magnetic helicity. Here N_c is the Coulomb number (Maruca et al. 2013; Kasper et al. 2017), which estimates the number of collisional timescales for protons. We calculate N_c using the proton–proton collision frequency, neglecting collisions between protons and other ions. We bin the data in $\log_{10}(\beta_p)$ and θ_{vB} using bins of width $\Delta \log_{10}(\beta_p) = 0.05$ and $\Delta\theta_{vB} = 5°$. We restrict our analysis to $0.01 \leqslant \beta_p \leqslant 10$ and include the full range of $\theta_{vB} = [0°, 180°]$ to account for any dependence on heliospheric sector structure. In Figure 2, we plot the probability density distribution of the data,

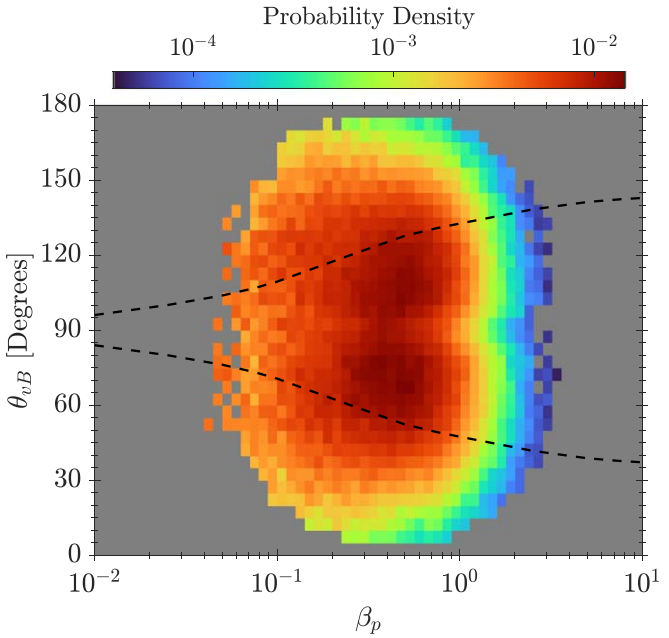

Figure 2. Probability density distribution of solar wind data in the β_p–θ_{vB} plane, calculated using Equation (18). The dashed black lines indicate the isocontours of $\tilde{\sigma}_m(\theta_{vB}) = 0$ mirrored about the line $\theta_{vB} = 90°$ (see main text).

$$\tilde{p} = \frac{n}{N \Delta\beta_p \Delta\theta_{vB}}, \tag{18}$$

in the β_p–θ_{vB} plane, where n is the number of data points in each bin and N is the total number of data points. We overplot the isocontour of $\sigma_m(\boldsymbol{k}) = 0$ from Figure 1(b) by replacing θ_{kB} with θ_{vB}, i.e., $\tilde{\sigma}_m(\theta_{vB}) = 0$. If we assume that the turbulence is independent of θ_{vB}, then any dependence on θ_{vB} exclusively reflects a dependence on θ_{kB} (see Horbury et al. 2008; Wicks et al. 2010; He et al. 2011; Podesta & Gary 2011a). We mirror the $\tilde{\sigma}_m(\theta_{vB}) = 0$ curve around the line $\theta_{vB} = 90°$ to account for heliospheric sector structure. The distribution of data in Figure 2 shows two peaks at $\theta_{vB} \sim 70°$ and $\theta_{vB} \sim 110°$ around $\beta_p \sim 0.5$. There are fewer data points at quasi-parallel angles, showing that the majority of data are associated with oblique angles. Naively, one would expect the distribution to follow the large-scale Parker spiral, peaking at angles ∼45° and ∼135°. However, we note that θ_{vB} is calculated at ∼92 s timescales, over which the local mean field $\boldsymbol{B}_0$ has already been deflected from the Parker spiral by Alfvénic fluctuations present at larger scales. There is also a clear β_p dependence in Figure 2, with the majority of the data lying in the range $0.1 \lesssim \beta_p \lesssim 1$, which is typical for quiescent solar wind (Wilson et al. 2018).

[12] See Table 1 in Woodham et al. (2019).
[13] See the Appendix in Woodham et al. (2018).

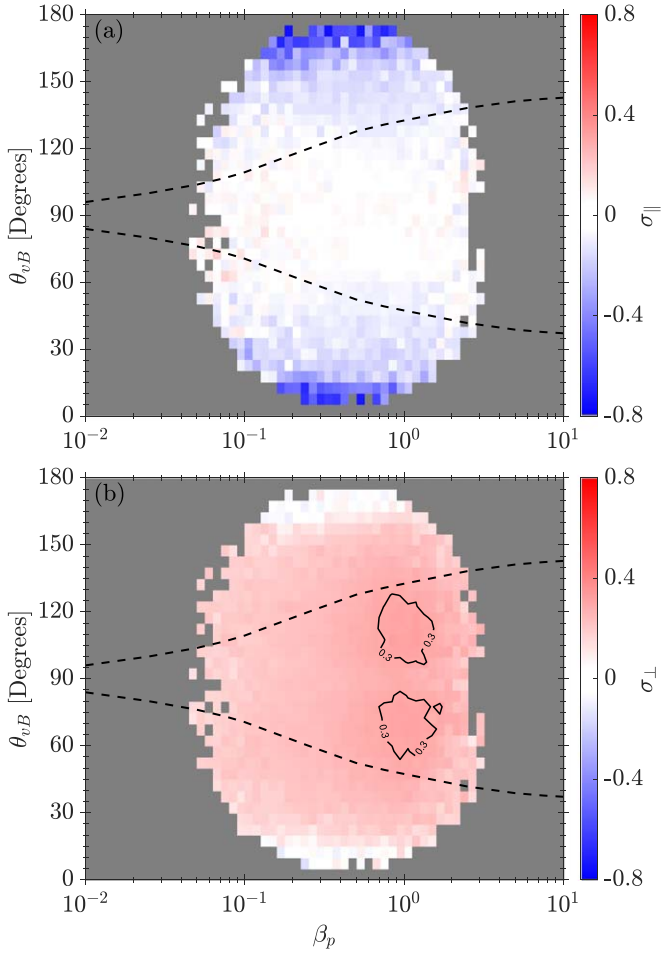

Figure 3. (a) Median $\sigma_\parallel$ and (b) median $\sigma_\perp$ across the β_p–θ_{vB} plane. The dashed black lines indicate the isocontours of $\tilde{\sigma}_m(\theta_{vB}) = 0$ mirrored about the line $\theta_{vB} = 90°$. We also include contours of constant $\sigma_\perp = 0.3$ in panel (b) as solid black lines.

5. Results

In Figure 3, we plot the median values of $\sigma_\parallel$ and $\sigma_\perp$ for each bin in the β_p–θ_{vB} plane. We neglect any bins with fewer than 20 data points to improve statistical reliability. From Figure 1, we expect to measure KAW-like fluctuations with $\sigma_\perp > 0$ in the area of the β_p–θ_{vB} plane enclosed by the two dashed lines at quasi-perpendicular angles, and AIC wave-like fluctuations with $\sigma_\parallel < 0$ at quasi-parallel angles. Figure 3 is consistent with this expectation; we see a strong negative helicity signal at $0° \leqslant \theta_{vB} \leqslant 30°$ and $150° \leqslant \theta_{vB} \leqslant 180°$, with a minimum of $\sigma_\parallel \simeq -0.8$ approaching $\theta_{vB} \simeq 0°$, as well as a weaker positive signal of $\sigma_\perp \simeq 0.4$ at angles $60° \leqslant \theta_{vB} \leqslant 120°$. Both $\sigma_\parallel$ and $\sigma_\perp$ are symmetrically distributed about the line $\theta_{vB} = 90°$ since we remove the ambiguity in the sign of the helicity due to the direction of $\boldsymbol{B}_0$. The distribution of $\sigma_\parallel$ is consistent with the presence of quasi-parallel-propagating AIC waves from kinetic instabilities in the solar wind (Zhao et al. 2018, 2019a; Woodham et al. 2019). Elsewhere in Figure 3(a), the median value of $\sigma_\parallel$ is zero, showing that a coherent signal of parallel-propagating fluctuations at ion-kinetic scales in the solar wind is not measured at oblique angles.

In Figure 3(b), there are two peaks in the median $\sigma_\perp$ close to $\beta_p \sim 1$, located at $\theta_{vB} \sim 70°$ and $\theta_{vB} \sim 110°$. Despite these peaks, the signal is spread across the parameter space, except at quasi-parallel angles where $\sigma_\perp \simeq 0$. We interpret this spread using Taylor's hypothesis. Due to the $\boldsymbol{k} \cdot \boldsymbol{v}_{\rm sw}$ term in the δ-function in Equation (9), a $\cos\theta_{kv}$ factor modifies the contribution of all modes to the reduced spectrum measured in the direction of $\boldsymbol{v}_{\rm sw}$. If $\theta_{kv} = 0°$, then $\cos\theta_{kv} = 1$, and the waves are measured at their actual k. However, oblique modes measured at a fixed $\omega_{\rm sc}$ correspond to a higher k in the plasma frame. Since the turbulent spectrum decreases in amplitude with increasing k, the reduced spectrum is most sensitive to the smallest $\boldsymbol{k}$ in the sampling direction. For parallel-propagating fluctuations such as AIC waves, $\theta_{vB} \simeq \theta_{kv}$, but for a broader k-distribution of obliquely propagating fluctuations, multiple fluctuations with different $\boldsymbol{k}$, and therefore different θ_{kB}, contribute to a single θ_{vB} bin. The signal at $\theta_{vB} \lesssim 30°$ is then likely due to fluctuations with $\theta_{kB} \gtrsim 60°$, since they contribute to $\sigma_\perp$, i.e., have a significant $k_\perp$ component.

As the polarization properties of small-scale Alfvénic fluctuations are consistent with predictions from linear theory, it is reasonable to expect that T_p is also correlated in the β_p–θ_{vB} plane. This expectation follows because different Alfvénic fluctuations are associated with different dissipation mechanisms, leading to distinct heating signatures. On the other hand, if the properties of the turbulence are truly independent of θ_{vB}, then we expect the dissipation mechanisms, and therefore proton heating, to be independent of θ_{vB}. To test this hypothesis, we plot the median values of $T_{p,\perp}/\langle T_{p,\perp}\rangle$ and $T_{p,\parallel}/\langle T_{p,\parallel}\rangle$ for each bin in the β_p–θ_{vB} plane in Figure 4. Here $\langle T_{p,\perp/\parallel}\rangle$ is the average value of $T_{p,\perp/\parallel}$ over all angles for each bin in $\log_{10}(\beta_p)$. This column normalization removes the systematic proportionality of T_p with β_p. The color of each bin in the θ_{vB}–β_p plane, therefore, shows as a function of θ_{vB} whether the proton temperature is equal to, larger than, or smaller than the average for a specific β_p.

Figure 4 shows a clear dependence of the median column-normalized $T_{p,\perp}$ and $T_{p,\parallel}$ on both θ_{vB} and β_p. In general, we see higher $T_{p,\perp}/\langle T_{p,\perp}\rangle$ at quasi-parallel angles where $\sigma_\parallel$ is largest in Figure 3(a), associated with AIC waves driven by kinetic instabilities (Kasper et al. 2002a; Matteini et al. 2007; Bale et al. 2009; Maruca et al. 2012; Woodham et al. 2019). We also see higher $T_{p,\parallel}/\langle T_{p,\parallel}\rangle$ at oblique angles where $\sigma_\perp$ is largest in Figure 3(b), associated with KAW-like fluctuations (Leamon et al. 1999; Bale et al. 2005; Howes et al. 2008; Sahraoui et al. 2010). However, there are also enhancements in $T_{p,\perp}/\langle T_{p,\perp}\rangle$ where $\sigma_\perp \simeq 0.3$, as indicated by the contours of constant $\sigma_\perp$ from Figure 3(b). Despite enhancements in both the column-normalized $T_{p,\perp}$ and $T_{p,\parallel}$ in this region of parameter space, the proton temperature remains anisotropic with $T_{p,\perp}/T_{p,\parallel} < 1$. We note that a lack of helicity signature does not imply that waves are not present. Therefore, if the enhancements in proton temperature are associated with different dissipation mechanisms, we do not expect a perfect correlation with $\sigma_\parallel$ and $\sigma_\perp$ in the θ_{vB}–β_p plane.

Hellinger & Trávníček (2014) recommend to exercise caution when bin-averaging solar wind data in a reduced parameter space. While conditional statistics have been employed in several studies (e.g., Bale et al. 2009; Maruca et al. 2011; Osman et al. 2012), this nontrivial procedure may give spurious results as a consequence of superposition of multiple correlations in the solar wind and should be interpreted cautiously. We find no evidence that the correlations shown in Figure 4 are caused by or related to other underlying correlations in the solar wind multidimensional parameter space. In particular, we rule out the known

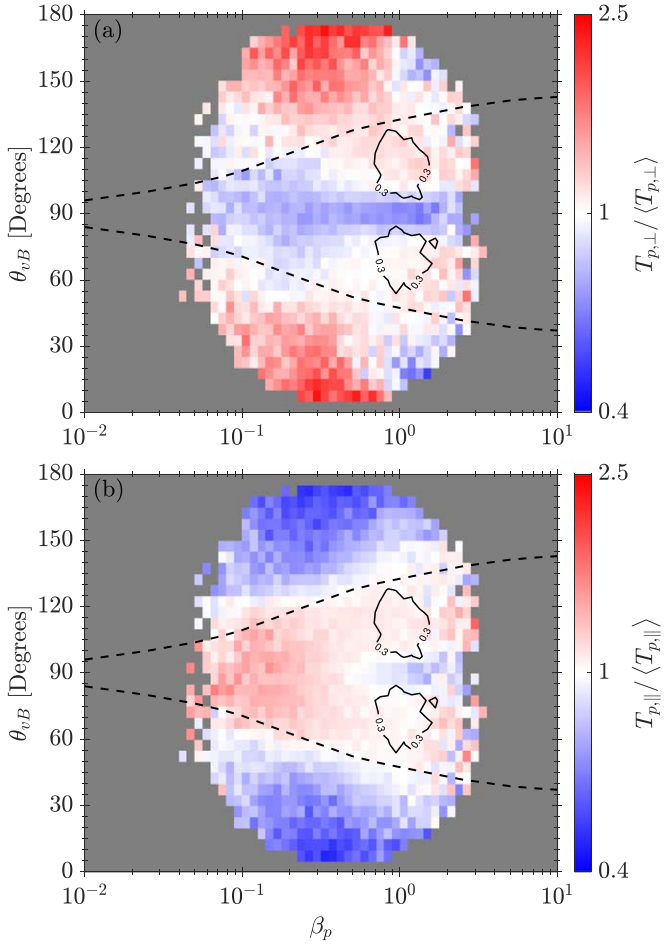

Figure 4. (a) Median proton perpendicular temperature, $T_{p,\perp}/\langle T_{p,\perp}\rangle$, and (b) median proton parallel temperature, $T_{p,\parallel}/\langle T_{p,\parallel}\rangle$, across β_p–θ_{vB} space. In both panels, we column-normalize the data by the median temperature in each β_p bin, $\langle T_{p,\perp/\parallel}\rangle$, to remove the systematic dependency of β_p on temperature. The dashed black lines indicate the isocontours of $\bar{\sigma}_m(\theta_{vB}) = 0$ mirrored about the line $\theta_{vB} = 90°$. We also include contours of constant $\sigma_\perp = 0.3$ from Figure 3(b) as black lines.

correlation between $v_{\rm sw}$ and T_p (Matthaeus et al. 2006; Perrone et al. 2019) by separating our results as a function of solar wind speed, finding that Figure 4 is largely unchanged (not shown). This is consistent with the fact that the β_p–θ_{vB} parameter space we investigate is determined by the properties of Alfvénic fluctuations, which exist in both fast and slow wind (e.g., D'Amicis et al. 2019b).

6. Discussion

It is well known that Alfvénic turbulence is anisotropic, its properties dependent on the angle θ_{kB}. For a single spacecraft sampling in time, the common assumption of ergodicity means that we measure a statistically similar distribution of turbulent fluctuations. Hence, by sampling along different directions relative to a changing θ_{vB}, we measure different components of the same distribution, e.g., the spectrum of magnetic fluctuations parallel and perpendicular to $\boldsymbol{B}_0$. The same is true for magnetic helicity, where the left- or right-handedness is determined only by the sampling direction. Certain fluctuations may still exist, and we do not measure them since we do not sample close enough to the $\boldsymbol{k}$ of these modes for them to make a significant contribution to the $\boldsymbol{k}\cdot\boldsymbol{v}_{\rm sw}$ term in Equation (9). Therefore, if turbulent dissipation is ongoing, we expect the resultant heating to exhibit the same distribution as the fluctuations at ion-kinetic scales. This is because the polarization properties of solar wind fluctuations affect what dissipation mechanisms can occur.

We initially hypothesized that the proton temperature would not exhibit a systematic dependence on either θ_{vB} or $\sigma_{\parallel,\perp}$. However, we show a clear dependence of $T_{p,\perp/\parallel}/\langle T_{p,\perp/\parallel}\rangle$ on θ_{vB} in Figure 4 that also correlates with the magnetic helicity signatures of different Alfvénic fluctuations at ion-kinetic scales. This result suggests that the properties of the turbulence also change with θ_{vB}. In other words, differences in the spectra of magnetic fluctuations with changing θ_{vB} are due to both single-spacecraft sampling effects and differences in the underlying distribution of turbulent fluctuations. If this interpretation is correct, studies that sample many angles θ_{vB} as the solar wind flows past a single spacecraft to build up a picture of the turbulence in the plasma, i.e., to sample different θ_{kB}, need to be interpreted very carefully (e.g., Horbury et al. 2008; Wicks et al. 2010; He et al. 2011; Podesta & Gary 2011a). In this study, we measure θ_{vB} at ∼92 s timescales, which suppresses large-scale correlations such as the Parker spiral. Instead, we show correlations between small-scale fluctuations with respect to a local mean field and the macroscopic proton temperature. Therefore, it is fair to assume that the dependence of $T_{p,\perp}/\langle T_{p,\perp}\rangle$ and $T_{p,\parallel}/\langle T_{p,\parallel}\rangle$ on θ_{vB} and β_p reflects the differences in the localized dissipation and heating processes at ion-kinetic scales in the solar wind.

A large enough $T_{p,\perp}/T_{p,\parallel}$ can drive AIC waves unstable in the solar wind (Kasper et al. 2002a; Matteini et al. 2007; Bale et al. 2009; Maruca et al. 2012). The driving of these waves is enhanced by the frequent presence of an α-particle proton differential flow or proton beam in the solar wind (Podesta & Gary 2011a, 2011b; Wicks et al. 2016; Woodham et al. 2019; Zhao et al. 2019b, 2020a). The enhancement in $T_{p,\perp}/\langle T_{p,\perp}\rangle$ at quasi-parallel angles in Figure 4(a) is likely responsible for the driving of these modes and correlates with the peak in $\sigma_\parallel$ at these angles in Figure 3(a), where we measure the strongest signal. While we are unable to observe AIC waves at oblique angles using a single spacecraft, we also measure KAW-like fluctuations at these angles using $\sigma_\perp$ in Figure 3(b). The peaks in $\sigma_\perp$ correlate with the observed enhancement in $T_{p,\perp}/\langle T_{p,\perp}\rangle$ and therefore are consistent with the dissipation of these fluctuations leading to perpendicular heating. A common dissipation mechanism proposed for KAW-like fluctuations is Landau damping (e.g., Howes 2008; Schekochihin et al. 2009); however, this leads to heating parallel to $\boldsymbol{B}_0$. Instead, perpendicular heating may arise from processes such as stochastic heating (Chandran et al. 2010, 2013) or even cyclotron resonance (Isenberg & Vasquez 2019), although more work is needed to confirm this.

We note that several studies (Markovskii & Vasquez 2013, 2016; Markovskii et al. 2016; Vasquez et al. 2018) show that nonlinear fluctuations confined to the plane perpendicular to $\boldsymbol{B}_0$ can produce the observed right-handed helicity signature in $\sigma_\perp$ in the same way as linear KAWs (e.g., Howes & Quataert 2010; He et al. 2012a). In this study, we refer to KAW-like fluctuations as nonlinear turbulent fluctuations with polarization properties that are consistent with linear KAWs, rather than linear modes. This interpretation does not preclude the possibility of resonant damping (Li et al. 2016, 2019; Klein et al. 2017, 2020; Howes et al. 2018; Chen

et al. 2019) or stochastic heating (e.g., Cerri et al. 2021) discussed above; however, additional processes cannot be ruled out. For example, kinetic simulations show perpendicular heating of ions by turbulent processes that may be unrelated to wave damping or stochastic heating, although the exact heating mechanism is still unclear (e.g., Parashar et al. 2009; Servidio et al. 2012; Vasquez 2015; Yang et al. 2017).

The variation of $T_{p,\parallel}/\langle T_{p,\parallel}\rangle$ in the β_p–θ_{vB} plane in Figure 4(b) is more difficult to interpret. This result could also be a signature of proton Landau damping of KAW-like fluctuations, although this process is typically stronger at $\beta_p \gtrsim 1$ (Gary & Nishimura 2004; Kawazura et al. 2019). While we measure fluctuations that can consistently explain the enhancement in $T_{p,\parallel}/\langle T_{p,\parallel}\rangle$, other fluctuations may be present that we do not measure. Direct evidence of energy transfer between the fluctuations and protons is needed to confirm this result, for example, using the field–particle correlation method (Klein & Howes 2016; Howes et al. 2017; Klein 2017; Klein et al. 2017; Chen et al. 2019; Li et al. 2019). This evidence will require higher-resolution data than provided by Wind. We note that caution must be given when interpreting these results, since several other effects may also explain the temperature dependence seen in the β_p–θ_{vB} plane. For example, instrumental effects and the role of solar wind expansion may result in similar temperature profiles. We now discuss these two effects in turn, showing that they cannot fully replicate our results presented in this paper.

7. Analysis Caveats

7.1. Instrumentation and Measurement Uncertainties

The SWE Faraday cups on board Wind measure a reduced VDF that is a function of the average direction of $\boldsymbol{B}_0$ over the measurement interval (Kasper 2002). As the spacecraft spins every 3 s in the ecliptic plane, the Faraday cups measure the current due to ions in several angular windows. The Faraday cups repeat this process using a different voltage (energy) window for each spacecraft rotation, building up a full spectrum every ∼92 s. By fitting a bi-Maxwellian to the reduced proton VDF, the proton thermal speeds, $w_{p,\parallel}$ and $w_{p,\perp}$, are obtained and converted to temperatures via $T_{p,\perp/\parallel} = m_p w_{p,\perp/\parallel}^2/2k_B$, where m_p is the proton mass. Due to the orientation of the cups on the spacecraft body, the direction of $\boldsymbol{B}_0$ with respect to the axis of the cups as they integrate over the proton VDF can cause inherent uncertainty in $w_{p,\parallel}$ and $w_{p,\perp}$. For example, if $\boldsymbol{B}_0$ is radial, then measurements of $w_{p,\parallel}$ have a smaller uncertainty compared to when the field is perpendicular to the cup, i.e., $\boldsymbol{B}_0$ is oriented out of the ecliptic plane by a significant angle, $\theta_{vB} \gtrsim 60°$ (Kasper et al. 2006). In Figure 5, we plot the percentage uncertainty in $w_{p,\parallel}$ and $w_{p,\perp}$,

$$U(w_{p,\perp/\parallel}) = \frac{\Delta w_{p,\perp/\parallel}}{w_{p,\perp/\parallel}} \times 100\%, \tag{19}$$

in the β_p–θ_{vB} plane, where $\Delta w_{p,\perp/\parallel}$ is the uncertainty in $w_{p,\perp/\parallel}$, derived from the nonlinear fitting of the distribution functions. We note that these uncertainties are not equivalent to Gaussian measurement errors; however, they provide a qualitative aid to understand systematic instrumental issues in the Faraday cup data.

We see that $w_{p,\perp}$ has a larger uncertainty (∼40%) at quasi-parallel angles in Figure 5(a), which is almost independent of β_p. While the median $T_{p,\perp}/\langle T_{p,\perp}\rangle$ in Figure 4(a) is larger at these angles, it exhibits a clear dependence on β_p. Therefore, increased uncertainty in the temperature measurements alone cannot completely account for the observed enhancement in $T_{p,\perp}/\langle T_{p,\perp}\rangle$ at these angles in the β_p–θ_{vB} plane. At quasi-perpendicular angles, the uncertainty in $w_{p,\perp}$ is less than 10%, suggesting that the enhancements in $T_{p,\perp}/\langle T_{p,\perp}\rangle$ in Figure 4(a) at $\beta_p \simeq 1$ and $40° \lesssim \theta_{vB} \lesssim 140°$ are unlikely to result from instrumental uncertainties. From Figure 5(b), the uncertainty in $w_{p,\parallel}$ is largest at $\theta_{vB} \simeq 90°$, although there is a larger spread to $70° \lesssim \theta_{vB} \lesssim 110°$ at $\beta_p \gtrsim 0.3$. By comparing with Figure 4(b), the enhancement in $T_{p,\parallel}/\langle T_{p,\parallel}\rangle$ over the entire β_p range does not coincide exactly with the regions of β_p–θ_{vB} space where these measurements have increased uncertainty. We also expect that any increased uncertainty in the $w_{p,\parallel}$ measurements would lead to increased noise that destroys any coherent median signal in this space, weakening the enhancement seen in Figure 4(b). Therefore, we conclude that the increased uncertainty in $w_{p,\parallel}$ at oblique angles is not the sole cause of the observed enhancement in $T_{p,\parallel}/\langle T_{p,\parallel}\rangle$.

Another source of uncertainty from the SWE measurements arises from the changing magnetic field direction over the course of the ∼92 s measurement interval (Maruca &

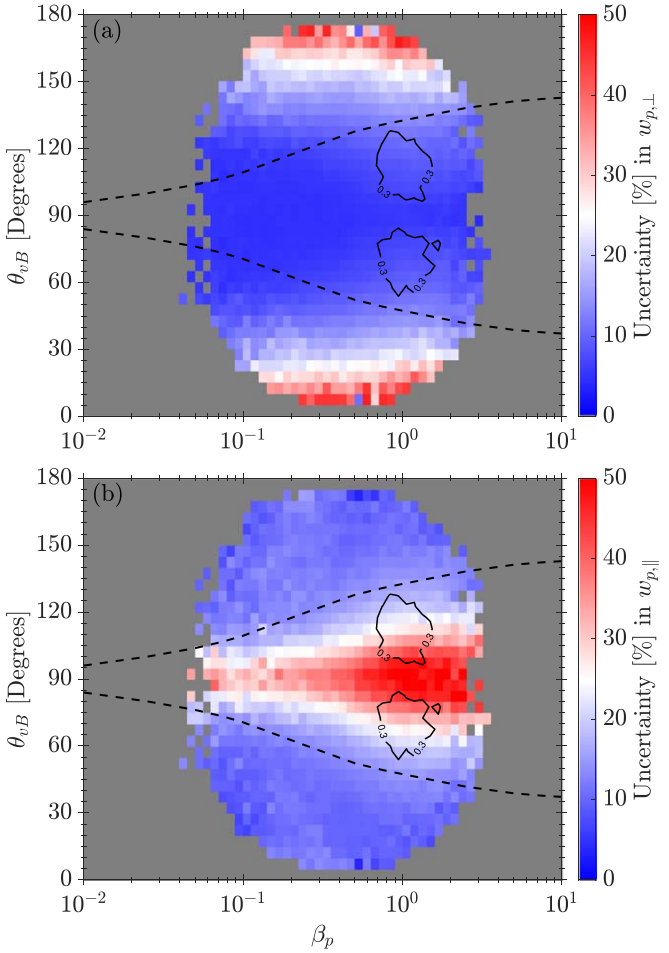

Figure 5. Median percentage uncertainty in (a) $w_{p,\perp}$ and (b) $w_{p,\parallel}$, across β_p–θ_{vB} space. The dashed black lines indicate the isocontours of $\tilde{\sigma}_m(\theta_{vB}) = 0$ mirrored about the line $\theta_{vB} = 90°$. We also include contours of constant $\sigma_\perp = 0.3$ from Figure 3(b) as black lines.

Kasper 2013). We quantify the angular fluctuations in $\boldsymbol{B}$ using

$$\psi_B = \sum_{i=1}^{N} \arccos(\hat{\boldsymbol{B}}_i \cdot \hat{\boldsymbol{B}}_{92})/N, \tag{20}$$

where N is the number of spacecraft rotations in a single measurement, $\hat{\boldsymbol{B}}_{92}$ is the average magnetic field direction over the whole measurement interval, and $\hat{\boldsymbol{B}}_i$ is the magnetic field unit vector averaged over each 3 s rotation. A large ψ_B can lead to the blurring of anisotropies in the proton thermal speeds. In other words, the fluctuations in $\boldsymbol{B}$ over the integration time result in a broadening of the reduced VDFs, increasing uncertainty in these measurements (see, e.g., Verscharen & Marsch 2011). To reduce this blurring effect, we remove SWE measurements with angular deviations $\psi_B > 15°$. Maruca (2012) provides an alternative data set of proton moments from SWE measurements to account for large deviations in the instantaneous magnetic field, using an average $\boldsymbol{B}_0$ over each voltage window scan (i.e., one rotation of the spacecraft, ∼3 s) to calculate $w_{p,\perp}$ and $w_{p,\parallel}$. Maruca & Kasper (2013) show that the Kasper (2002) data set often underestimates the temperature anisotropy of proton VDFs. Our comparison with this alternative data set (not shown here) reveals that both $T_{p,\perp}/\langle T_{p,\perp}\rangle$ and $T_{p,\parallel}/\langle T_{p,\parallel}\rangle$ show a similar, albeit slightly reduced, dependence on both β_p and θ_{vB}. This result suggests that the temperature dependence we see in the β_p–θ_{vB} plane is unlikely to be caused by the blurring of proton temperature anisotropy measurements.

7.2. CGL Spherical Expansion

Another possible source of proton temperature dependence on θ_{vB} is the expansion of the solar wind as it flows out into the heliosphere. The double adiabatic closure presented by Chew et al. (1956) predicts the evolution of $T_{p,\perp}$ and $T_{p,\parallel}$ assuming no collisions, negligible heat flux, and no local heating:

$$\frac{d}{dt}\left(\frac{T_{p,\perp}}{B}\right) = 0 \quad \text{and} \quad \frac{d}{dt}\left(\frac{T_{p,\parallel}B^2}{n_p^2}\right) = 0, \tag{21}$$

where d/dt is the convective derivative. Under the assumption of steady-state spherical expansion, which is purely transverse to the radial direction with a constant radial velocity, $\boldsymbol{v}_{\rm sw} = v_{\rm sw}\,\hat{\boldsymbol{R}}$, the continuity equation gives $n_p \propto 1/r^2$, where r is the radial distance from the Sun. We assume that the radial evolution of the magnetic field in the equatorial plane follows the Parker spiral (Parker 1958),

$$B \propto \frac{\sqrt{\cos^2\phi_0 + r^2\sin^2\phi_0}}{r^2}, \tag{22}$$

which gives a radial dependence of $B \propto 1/r^2$ when $\phi_0 = 0°$ and $B \propto 1/r$ when $\phi_0 = 90°$. The angle, ϕ_0, is the footpoint longitude of the field at the solar wind source surface, given by

$$\phi_0 = \arctan\left(\frac{r_0\Omega_\odot}{v_{\rm sw}}\right), \tag{23}$$

where $\Omega_\odot = 2.85 \times 10^{-6}$ rad s^{-1} is the constant solar angular rotation rate and $r_0 \simeq 20R_\odot$ (Owens & Forsyth 2013). Therefore, a value of $v_{\rm sw}$ sets the value of ϕ_0 at a given radius, r_0.

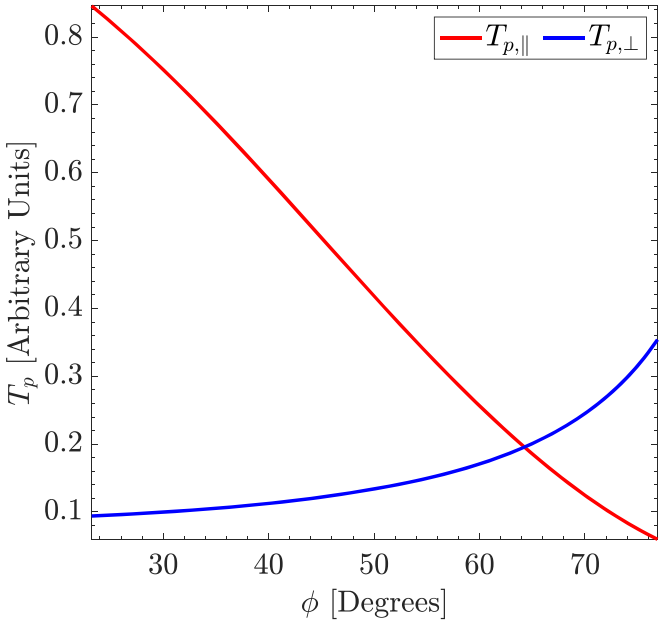

Figure 6. Temperature profiles $T_{p,\parallel}$ and $T_{p,\perp}$ as functions of ϕ at $r \simeq 1$ au for CGL spherical expansion given by Equations (24) and (25).

Then, $\phi = \tan^{-1}(B_\phi/B_r)$ is the azimuthal angle of $\boldsymbol{B}$ in the equatorial plane at a distance, r, from the Sun. The two angles are related by $\tan\phi = R\tan\phi_0$, where $R = r/r_0$. From Equations (21) and (22) and the radial dependence of n_p, we obtain

$$\frac{T_{p,\perp}}{T_{0,\perp}} = \frac{\sqrt{\cos^2(\phi_0) + R^2\sin^2(\phi_0)}}{R^2} \tag{24}$$

and

$$\frac{T_{p,\parallel}}{T_{0,\parallel}} = \frac{1}{\cos^2(\phi_0) + R^2\sin^2(\phi_0)}, \tag{25}$$

where $T_{0,\perp}$ and $T_{0,\parallel}$ are the perpendicular and parallel proton temperatures at r_0, respectively. We use Equations (24) and (25) to investigate the dependence of proton temperature on ϕ at $r = 215R_\odot \simeq 1$ au. Since the solar wind velocity is radial, the angle ϕ is approximately equal to θ_{vB}. We set $T_{0,\perp} = 10$ and $T_{0,\parallel} = 1$, giving $R = 10.75$ for $r_0 = 20R_\odot$. We create a distribution of angles ϕ_0 using Equation (23) by selecting a range of wind speeds: 100 km s$^{-1} \leqslant v_{\rm sw} \leqslant 1000$ km s^{-1}. This range of ϕ_0 gives $20° \lesssim \phi \lesssim 80°$ at 1 au. In Figure 6, we show the variation of $T_{p,\perp}$ and $T_{p,\parallel}$ with ϕ. We choose a larger $T_{\perp,0}$ to show more clearly the variation in $T_{p,\perp}$. We see that $T_{p,\parallel}$ remains similar to the value set close to the Sun (small ϕ) and decreases rapidly with increasing ϕ, approaching zero at $\phi \gtrsim 70°$. On the other hand, $T_{p,\perp}$ is largest at $\phi \gtrsim 60°$ and approaches 0.1 for $\phi \lesssim 30°$. This dependence of $T_{p,\perp}$ and $T_{p,\parallel}$ is opposite to what we observe in Figure 4, which in general shows larger $T_{p,\parallel}$ at $\theta_{vB} \simeq 90°$ and larger $T_{p,\perp}$ at $\theta_{vB} \simeq 0°$. Therefore, spherical expansion alone cannot explain our results.

8. Conclusions

We use magnetic helicity to investigate the polarization properties of Alfvénic fluctuations with finite radial wavenumber, k_r, at ion-kinetic scales in the solar wind. Using almost 15 yr of Wind observations, we separate the contributions to helicity from fluctuations with wavevectors quasi-parallel and oblique to $\boldsymbol{B}_0$, finding that the helicity of Alfvénic fluctuations is consistent with predictions from linear Vlasov theory. In particular, the peak in magnetic helicity at ion-kinetic scales and its variation with β_p and θ_{vB} shown in Figure 3 are in agreement with the dispersion relation of linear Alfvén waves (Gary 1986), when modified by Taylor's hypothesis. This result suggests that the nonlinear turbulent fluctuations at these scales share at least some polarization properties with Alfvén waves.

We also investigate the dependence of local kinetic heating processes due to turbulent dissipation on θ_{vB}. In Figure 4, we find that both $T_{p,\perp}$ and $T_{p,\parallel}$, when normalized to their average value in each β_p-bin, show a clear dependence on θ_{vB}. The temperature parallel to $\boldsymbol{B}_0$ is generally higher in the parameter space where we measure a coherent helicity signature associated with KAW-like fluctuations, and perpendicular temperature higher in the parameter space where we measure a signature expected from AIC waves. We also see small enhancements in the perpendicular temperature where we measure the strongest helicity signal of KAW-like fluctuations. However, we reiterate the important fact that the lack of a wave signal is not the same as a lack of presence of waves.

Our results suggest that the properties of turbulent fluctuations at ion-kinetic scales in the solar wind depend on the angle θ_{vB}. This finding is inconsistent with the general assumption that sampling different θ_{vB} allows us to sample different parts of the same ensemble of fluctuations that is otherwise unaltered in its statistical properties. Therefore, studies that sample different θ_{vB} in order to sample different θ_{kB} need to be interpreted very carefully. Instead, if we assume that the dissipation mechanisms and proton heating depend on θ_{vB}, the enhancements in proton temperature in Figure 4 are consistent with the role of wave–particle interactions in determining proton temperature in the solar wind. For example, whenever we measure the helicity of AIC waves or KAW fluctuations, then we also measure enhancements in proton temperature. However, the inverse is not necessarily true. We suggest that heating mechanisms associated with KAWs lead to both parallel (Howes 2008; Schekochihin et al. 2009) and perpendicular (Chandran et al. 2010, 2013; Isenberg & Vasquez 2019) heating. We rule out both instrumental and large-scale expansion effects, finding that neither of them alone can explain the observed temperature profile in the β_p–θ_{vB} plane.

In summary, our observations suggest that the properties of Alfvénic fluctuations at ion-kinetic scales determine the level of proton heating from turbulent dissipation. This interpretation is consistent with recent studies showing that larger magnetic helicity signatures at ion-kinetic scales are associated with larger proton temperatures and steeper spectral exponents (Pine et al. 2020; Zhao et al. 2020b, 2021). Our findings, therefore, provide new evidence for the importance of local kinetic processes in determining proton temperature in the solar wind. We emphasize that our conclusions do not invoke causality, just correlation. For example, we cannot rule out a lack of cooling rather than heating. However, while the adiabatic expansion of the solar wind causes the temperature to vary with θ_{vB}, this cannot explain the observed temperature profiles in the β_p–θ_{vB} plane. Further work is ongoing in order to confirm these results and develop a theory for the processes associated with the polarization properties of Alfvénic fluctuations that lead to the observed temperature profiles.

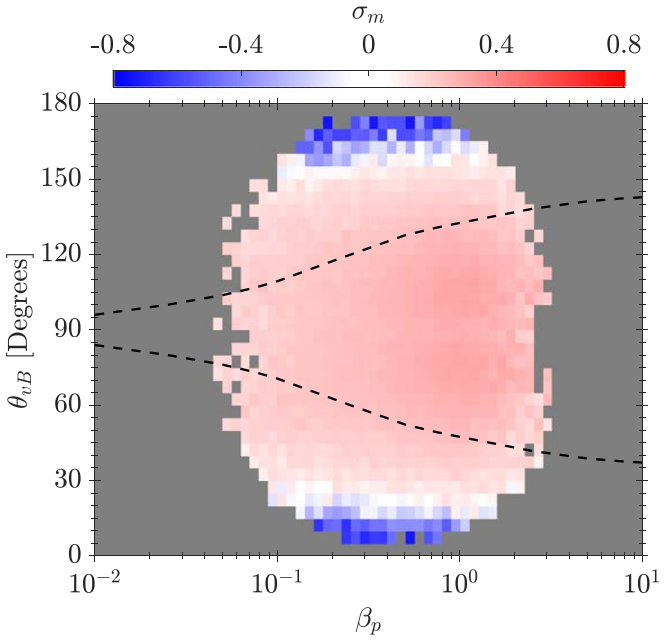

Figure 7. Median value of the peak in $\sigma_m^r(k_r)$ across the β_p–θ_{vB} plane. The dashed black lines indicate the isocontours of $\tilde{\sigma}_m(\theta_{vB}) = 0$ mirrored about the line $\theta_{vB} = 90°$.

L.D.W. thanks B. Alterman, L. Matteini, D. Stansby, and J. Stawarz for useful comments and discussions. L.D.W. is also grateful to B. Maruca for sharing his processed SWE data set for validation testing. L.D.W. was supported by an STFC studentship at UCL/MSSL ST/N504488/1 and the STFC consolidated grant ST/S000364/1 to Imperial College London; D.V. was supported by STFC Ernest Rutherford Fellowship ST/P003826/1; R.T.W. was supported by the STFC consolidated grants to UCL/MSSL, ST/N000722/1 and ST/S000240/1. J.M.T. was supported by an NSF SHINE award (AGS-1622306). G.G.H. was supported by NASA grants 80NSSC18K1217 and 80NSSC18K0643. All data from the Wind spacecraft used in this study are publicly available and were obtained from the NASA SPDF website.[14] The NHDS code is available at https://github.com/danielver02/NHDS.

Appendix
Decomposition of Fluctuating Magnetic Helicity

Here we present a mathematical derivation that decomposes $\sigma_m^r(k_r)$ into the different contributions, $\sigma_{ij}(k_l)$, calculated using Equation (13) (see also Wicks et al. 2012). In Figure 7 we plot the median value of the peak in $\sigma_m^r(k_r)$ across the β_p–θ_{vB} plane, showing two helicity signatures of opposite handedness. This technique allows us to separate the helicity signatures of different fluctuations at ion-kinetic scales in the solar wind, as we show in Figure 3.

[14] http://spdf.gsfc.nasa.gov

We consider a spacecraft that samples a single mode with wavevector

$$\boldsymbol{k} = k_\perp \cos\alpha\, \hat{\boldsymbol{x}} + k_\perp \sin\alpha\, \hat{\boldsymbol{y}} + k_\parallel \hat{\boldsymbol{z}}, \tag{A1}$$

where α is the azimuthal angle of $\boldsymbol{k}$ in the x–y plane. The full signal from turbulence corresponds to a superposition of the signals from each of the modes, so considering a single mode is sufficient to understand how the components $\sigma_{ij}(k_l)$ are related to $\sigma^r_m(k_r)$. Without loss of generality, we take the solar wind velocity to be in the x–z plane,

$$\boldsymbol{v}_{\rm sw} = v_{\rm sw} \sin\theta_{vB}\, \hat{\boldsymbol{x}} + v_{\rm sw} \cos\theta_{vB}\, \hat{\boldsymbol{z}}, \tag{A2}$$

and the local mean magnetic field to be $\boldsymbol{B}_0 = B_0\, \hat{\boldsymbol{z}}$. We use the relation $2\,\mathrm{Im}\,\{a^* b\} \equiv i(ab^* - a^* b)$ to rewrite $H'^r_m(k_r)$ in RTN coordinates from Equation (7) into the form

$$H'^r_m(k_r) = i\frac{\delta B_T\, \delta B_N^* - \delta B_T^*\, \delta B_N}{k_r}. \tag{A3}$$

The normalized reduced fluctuating magnetic helicity, $\sigma^r_m(k_r)$, is then given by Equation (11). We define the relation between the RTN and the field-aligned (Equation (12)) coordinate systems using the unit vector along the sampling direction, $\hat{\boldsymbol{v}}_{\rm sw} = \boldsymbol{v}_{\rm sw}/|\boldsymbol{v}_{\rm sw}|$:

$$\begin{aligned}
&\hat{\boldsymbol{R}} = \hat{\boldsymbol{v}}_{\rm sw} = \sin\theta_{vB}\hat{\boldsymbol{x}} + \cos\theta_{vB}\hat{\boldsymbol{z}};\\
&\hat{\boldsymbol{T}} = \hat{\boldsymbol{B}}_0 \times \hat{\boldsymbol{v}}_{\rm sw}/|\hat{\boldsymbol{B}}_0 \times \hat{\boldsymbol{v}}_{\rm sw}| = \hat{\boldsymbol{y}};\\
&\hat{\boldsymbol{N}} = \hat{\boldsymbol{R}} \times \hat{\boldsymbol{T}} = -\cos\theta_{vB}\hat{\boldsymbol{x}} + \sin\theta_{vB}\hat{\boldsymbol{z}}.
\end{aligned} \tag{A4}$$

By substituting for the RTN unit vectors in terms of $\hat{\boldsymbol{x}}$, $\hat{\boldsymbol{y}}$, and $\hat{\boldsymbol{z}}$ and simplifying, we obtain

$$\begin{aligned}
\sigma^r_m(k_r) = \frac{1}{|\delta\boldsymbol{B}(k_r)|^2}\Bigg\{&\left[\frac{i(\delta B_x \delta B_y^* - \delta B_x^* \delta B_y)}{k_z}\right] k_z \cos\theta_{vB}\\
&+ \left[\frac{i(\delta B_x \delta B_z^* - \delta B_x^* \delta B_z)}{k_y}\right] k_y \sin\theta_{vB}\sin\alpha\\
&+ \left[\frac{i(\delta B_y \delta B_z^* - \delta B_y^* \delta B_z)}{k_x}\right] k_x \sin\theta_{vB}\cos\alpha\Bigg\}.
\end{aligned} \tag{A5}$$

By defining the nonreduced fluctuating magnetic helicity (see also Equation (5)) as

$$\begin{aligned}
H'_m(\boldsymbol{k}) &= i\frac{\delta B_x \delta B_y^* - \delta B_x^* \delta B_y}{k_z}\\
&\equiv i\frac{\delta B_y \delta B_z^* - \delta B_y^* \delta B_z}{k_x}\\
&\equiv i\frac{\delta B_z \delta B_x^* - \delta B_z^* \delta B_x}{k_y},
\end{aligned} \tag{A6}$$

we can manipulate Equation (A5) into the form

$$\begin{aligned}
\sigma^r_m(k_r) &= \frac{H'_m(\boldsymbol{k})}{|\delta\boldsymbol{B}(k_r)|^2}\{k_z \cos\theta_{vB} - k_y \sin\theta_{vB}\sin\alpha\\
&\quad + k_x \sin\theta_{vB}\cos\alpha\},\\
&\equiv \sigma_{xy}(k_z)\cos\theta_{vB} + \sigma_{xz}(k_y)\sin\theta_{vB}\sin\alpha\\
&\quad + \sigma_{yz}(k_x)\sin\theta_{vB}\cos\alpha,
\end{aligned} \tag{A7}$$

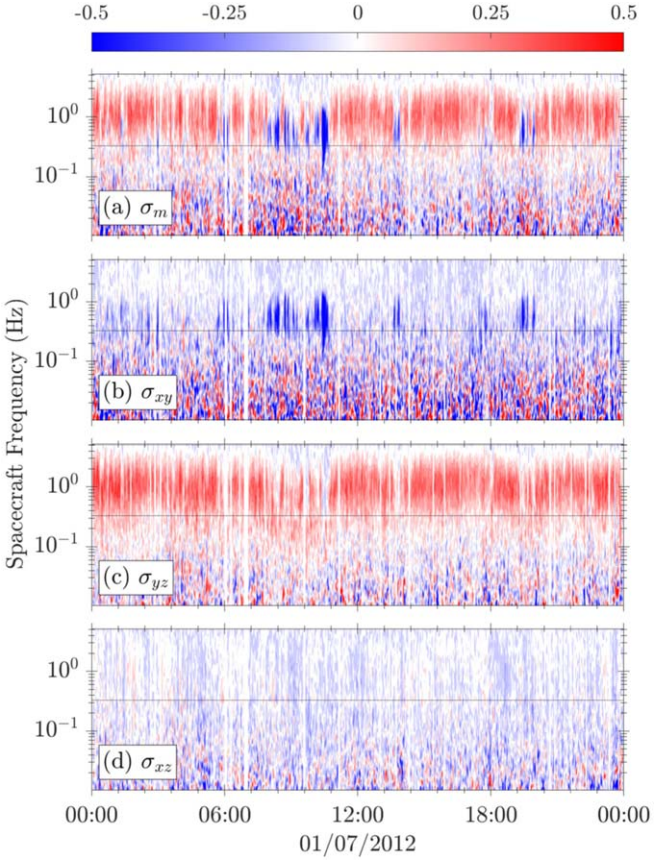

Figure 8. (a) Time series of reduced normalized fluctuating magnetic helicity spectra, σ^r_m, for a day of observations on 2012 July 1, and the different contributions to the total helicity, (b) σ_{xy}, (c) σ_{yz}, and (d) σ_{xz}. We plot the spectra as functions of the frequency in the spacecraft frame, $f_{\rm sc} = \omega_{\rm sc}/2\pi$. The black dashed line in panel (d) is the spacecraft spin frequency, 0.33 Hz.

where we define the different contributions, $\sigma_{ij}(k_l)$, using Equation (13). We equate each of the terms between the two forms in Equation (A7) to obtain the following direct relations between $\sigma^r_m(k_r)$ and $\sigma_{xy}(k_z)$, $\sigma_{xz}(k_y)$, and $\sigma_{yz}(k_x)$:

$$\sigma_{xy}(k_z) = \frac{H'_m(\boldsymbol{k})}{|\delta\boldsymbol{B}(k_r)|^2} k_z = \sigma^r_m(k_r)\frac{k_z}{k_r}, \tag{A8}$$

$$\sigma_{xz}(k_y) = -\frac{H'_m(\boldsymbol{k})}{|\delta\boldsymbol{B}(k_r)|^2} k_y = -\sigma^r_m(k_r)\frac{k_y}{k_r}, \tag{A9}$$

and,

$$\sigma_{yz}(k_x) = \frac{H'_m(\boldsymbol{k})}{|\delta\boldsymbol{B}(k_r)|^2} k_x = \sigma^r_m(k_r)\frac{k_x}{k_r}, \tag{A10}$$

which are the same as Equations (14), (15), and (16).

To highlight the separation of different fluctuations in the solar wind using this technique, we show in Figure 8(a) a time series of magnetic helicity spectra, σ^r_m, measured by Wind on 2012 July 1. We plot the spectra as functions of frequency in the spacecraft frame, $f_{\rm sc} = \omega_{\rm sc}/2\pi$ (see Equation (10)). In panels (b)–(d), we also plot σ_{ij}, showing the decomposition of σ^r_m into its three components. The two coherent signatures of opposite handedness at $f_{\rm sc} \simeq 1$ Hz in panel (a) are completely separated into the components σ_{xy} and σ_{yz} in panels (b) and (c). In panel (d), we see only small enhancements close to 0.33 Hz, which corresponds to the spin frequency of the spacecraft. Besides

this spacecraft artifact, there is no coherent helicity signature in σ_{xz}, as expected.

ORCID iDs

L. D. Woodham https://orcid.org/0000-0003-2845-4250
R. T. Wicks https://orcid.org/0000-0002-0622-5302
D. Verscharen https://orcid.org/0000-0002-0497-1096
J. M. TenBarge https://orcid.org/0000-0003-0143-951X
G. G. Howes https://orcid.org/0000-0003-1749-2665

References

Alexandrova, O., Chen, C. H. K., Sorriso-Valvo, L., Horbury, T. S., & Bale, S. D. 2013, SSRv, 178, 101
Alfvén, H. 1942, Natur, 150, 405
Alterman, B. L., Kasper, J. C., Stevens, M. L., & Koval, A. 2018, ApJ, 864, 112
Bale, S. D., Kasper, J. C., Howes, G. G., et al. 2009, PhRvL, 103, 211101
Bale, S. D., Kellogg, P. J., Mozer, F. S., Horbury, T. S., & Reme, H. 2005, PhRvL, 94, 215002
Barnes, A. 1981, JGR, 86, 7498
Batchelor, G. K. 1970, The Theory of Homogenous Turbulence (Cambridge: Cambridge Univ. Press)
Belcher, J. W., & Davis, L., Jr. 1971, JGR, 76, 3534
Belcher, J. W., Davis, L., Jr., & Smith, E. J. 1969, JGR, 74, 2302
Boldyrev, S., & Perez, J. C. 2012, ApJL, 758, L44
Bourouaine, S., Marsch, E., & Neubauer, F. M. 2010, GeoRL, 37, L14104
Bourouaine, S., Verscharen, D., Chandran, B. D., Maruca, B. A., & Kasper, J. C. 2013, ApJL, 777, L3
Bruno, R., & Carbone, V. 2013, LRSP, 10, 2
Bruno, R., & Telloni, D. 2015, ApJL, 811, L17
Cerri, S. S., Arzamasskiy, L., & Kunz, M. W. 2021, arXiv:2102.09654
Chandran, B. D. G., Li, B., Rogers, B. N., Quataert, E., & Germaschewski, K. 2010, ApJ, 720, 503
Chandran, B. D. G., Verscharen, D., Quataert, E., et al. 2013, ApJ, 776, 45
Chen, C. H. K., Klein, K. G., & Howes, G. G. 2019, NatCo, 10, 740
Chen, C. H. K., Mallet, A., Schekochihin, A. A., et al. 2012, ApJ, 758, 120
Chen, C. H. K., Mallet, A., Yousef, T. A., Schekochihin, A. A., & Horbury, T. S. 2011, MNRAS, 415, 3219
Chen, C. H. K. 2016, JPlPh, 82, 535820602
Chew, G. F., Goldberger, M. L., & Low, F. E. 1956, RSPSA, 236, 112
Coleman, P. J. 1968, ApJ, 153, 371
D'Amicis, R., & Bruno, R. 2015, ApJ, 805, 84
D'Amicis, R., De Marco, R., Bruno, R., & Perrone, D. 2019a, A&A, 632, A92
D'Amicis, R., Matteini, L., & Bruno, R. 2019b, MNRAS, 483, 4665
Forman, M. A., Wicks, R. T., & Horbury, T. S. 2011, ApJ, 733, 76
Fredricks, R. W., & Coroniti, F. V. 1976, JGR, 81, 5591
Galtier, S. 2006, JPlPh, 72, 721
Galtier, S., & Buchlin, E. 2007, ApJ, 656, 560
Gary, S. P. 1986, JPlPh, 35, 431
Gary, S. P. 1993, Theory of Space Plasma Microinstabilities (Cambridge: Cambridge Univ. Press)
Gary, S. P., & Borovsky, J. E. 2004, JGRA, 109, A06105
Gary, S. P., Jian, L. K., Broiles, T. W., et al. 2015, JGRA, 121, 30
Gary, S. P., & Nishimura, K. 2004, JGRA, 109, A02109
He, J., Marsch, E., Tu, C., Yao, S., & Tian, H. 2011, ApJ, 731, 85
He, J., Tu, C., Marsch, E., & Yao, S. 2012a, ApJ, 749, 86
He, J., Tu, C., Marsch, E., & Yao, S. 2012b, ApJL, 745, L8
Hellinger, P., & Trávníček, P. M. 2014, ApJL, 784, L15
Hellinger, P., Trávníček, P. M., Kasper, J. C., & Lazarus, A. J. 2006, GeoRL, 33, L09101
Horbury, T. S., Forman, M. A., & Oughton, S. 2008, PhRvL, 101, 175005
Horbury, T. S., Matteini, L., & Stansby, D. 2018, MNRAS, 478, 1980
Howes, G. G. 2008, PhPl, 15, 1
Howes, G. G., Bale, S. D., Klein, K. G., et al. 2012, ApJL, 753, 2
Howes, G. G., Cowley, S. C., Dorland, W., et al. 2006, ApJ, 651, 590
Howes, G. G., Dorland, W., Cowley, S. C., et al. 2008, PhRvL, 100, 065004
Howes, G. G., Klein, K. G., & Li, T. C. 2017, JPlPh, 83, 705830102
Howes, G. G., Klein, K. G., & Tenbarge, J. M. 2014, ApJ, 789, 106
Howes, G. G., McCubbin, A. J., & Klein, K. S. G. 2018, JPlPh, 84, 905840105
Howes, G. G., & Quataert, E. 2010, ApJL, 709, L49
Isenberg, P. A., & Vasquez, B. J. 2019, ApJ, 887, 63
Kasper, J. C. 2002, PhD thesis, Massachusetts Institute of Technology
Kasper, J. C., Klein, K. G., Weber, T., et al. 2017, ApJ, 849, 126
Kasper, J. C., Lazarus, A. J., & Gary, S. P. 2002a, GeoRL, 29, 20
Kasper, J. C., Lazarus, A. J., & Gary, S. P. 2002b, GeoRL, 29, 1839
Kasper, J. C., Lazarus, A. J., & Gary, S. P. 2008, PhRvL, 101, 261103
Kasper, J. C., Lazarus, A. J., Steinberg, J. T., Ogilvie, K. W., & Szabo, A. 2006, JGRA, 111, A03105
Kasper, J. C., Maruca, B. A., Stevens, M. L., & Zaslavsky, A. 2013, PhRvL, 110, 091102
Kawazura, Y., Barnes, M., & Schekochihin, A. A. 2019, PNAS, 116, 771
Klein, K. G. 2017, PhPl, 24, 055901
Klein, K. G., Alterman, B. L., Stevens, M. L., Vech, D., & Kasper, J. C. 2018, PhRvL, 120, 205102
Klein, K. G., & Howes, G. G. 2015, PhPl, 22, 032903
Klein, K. G., & Howes, G. G. 2016, ApJL, 826, L30
Klein, K. G., Howes, G. G., Tenbarge, J. M., et al. 2012, ApJ, 755, 159
Klein, K. G., Howes, G. G., & TenBarge, J. M. 2014a, ApJL, 790, L20
Klein, K. G., Howes, G. G., & TenBarge, J. M. 2017a, JPlPh, 83, 1
Klein, K. G., Howes, G. G., TenBarge, J. M., & Podesta, J. J. 2014b, ApJ, 785, 138
Klein, K. G., Howes, G. G., Tenbarge, J. M., & Valentini, F. 2020, JPlPh, 86, 905860402
Klein, K. G., Martinović, M., Stansby, D., & Horbury, T. S. 2019, ApJ, 887, 234
Koval, A., & Szabo, A. 2013, in AIP Conf. Proc. 1539: SOLAR WIND 13: Proc. of the 13th Int. Solar Wind Conf. (Melville, NY: AIP), 211
Leamon, R. J., Smith, C. W., Ness, N. F., & Wong, H. K. 1999, JGRA, 104, 22331
Lepping, R. P., Acuña, M. H., Burlaga, L. F., et al. 1995, SSRv, 71, 207
Li, T. C., Howes, G. G., Klein, K. G., Liu, Y.-H., & TenBarge, J. M. 2019, JPlPh, 85, 905850406
Li, T. C., Howes, G. G., Klein, K. G., & TenBarge, J. M. 2016, ApJL, 832, L24
MacBride, B. T., Smith, C. W., & Vasquez, B. J. 2010, JGRA, 115, A07105
Markovskii, S. A., & Vasquez, B. J. 2013, ApJ, 768, 62
Markovskii, S. A., & Vasquez, B. J. 2016, ApJ, 820, 15
Markovskii, S. A., Vasquez, B. J., & Smith, C. W. 2016, ApJ, 833, 212
Marsch, E. 2006, LRSP, 3, 1
Marsch, E. 2012, SSRv, 172, 23
Marsch, E., Goertz, C. K., & Richter, K. 1982, JGR, 87, 5030
Marsch, E., Vocks, C., & Tu, C. Y. 2003, NPGeo, 10, 101
Maruca, B. 2012, PhD thesis, Harvard University
Maruca, B. A., Bale, S. D., Sorriso-Valvo, L., Kasper, J. C., & Stevens, M. L. 2013, PhRvL, 111, 241101
Maruca, B. A., & Kasper, J. C. 2013, AdSpR, 52, 723
Maruca, B. A., Kasper, J. C., & Bale, S. D. 2011, PhRvL, 107, 201101
Maruca, B. A., Kasper, J. C., & Gary, S. P. 2012, ApJ, 748, 137
Matteini, L., Hellinger, P., Landi, S., Trávníček, P. M., & Velli, M. 2012, SSRv, 172, 373
Matteini, L., Horbury, T. S., Neugebauer, M., & Goldstein, B. E. 2014, GeoRL, 41, 259
Matteini, L., Horbury, T. S., Pantellini, F., Velli, M., & Schwartz, S. J. 2015, ApJ, 802, 11
Matteini, L., Landi, S., Hellinger, P., et al. 2007, GeoRL, 34, L20105
Matthaeus, W. H., Elliott, H. A., & McComas, D. J. 2006, JGRA, 111, A10103
Matthaeus, W. H., & Goldstein, M. L. 1982a, JGR, 87, 6011
Matthaeus, W. H., & Goldstein, M. L. 1982b, JGR, 87, 10347
Matthaeus, W. H., Goldstein, M. L., & Smith, C. W. 1982, PhRvL, 48, 1256
Montgomery, M. D., & Turner, L. 1981, PhFl, 24, 825
Ogilvie, K. W., Chornay, D. J., Fritzenreiter, R. J., et al. 1995, SSRv, 71, 55
Osman, K. T., Matthaeus, W. H., Hnat, B., & Chapman, S. C. 2012, PhRvL, 108, 261103
Owens, M. J., & Forsyth, R. J. 2013, LRSP, 10, 5
Parashar, T. N., Shay, M. A., Cassak, P. A., & Matthaeus, W. H. 2009, PhPl, 16, 032310
Parker, E. N. 1958, ApJ, 128, 664
Perri, S., & Balogh, A. 2010, ApJ, 714, 937
Perri, S., Goldstein, M. L., Dorelli, J. C., & Sahraoui, F. 2012, PhRvL, 109, 191101
Perrone, D., D'Amicis, R., De Marco, R., et al. 2020, A&A, 633, A166
Perrone, D., Stansby, D., Horbury, T. S., & Matteini, L. 2019, MNRAS, 488, 2380
Pine, Z. B., Smith, C. W., Hollick, S. J., et al. 2020, ApJ, 900, 91
Podesta, J. J., & Gary, S. P. 2011a, ApJ, 734, 15
Podesta, J. J., & Gary, S. P. 2011b, ApJ, 742, 41
Šafránková, J., Němeček, Z., Němec, F., et al. 2019, ApJ, 870, 40
Sahraoui, F., Goldstein, M. L., Belmont, G., Canu, P., & Rezeau, L. 2010, PhRvL, 105, 131101

Schekochihin, A. A., Cowley, S. C., Dorland, W., et al. 2009, ApJS, 182, 310
Servidio, S., Valentini, F., Califano, F., & Veltri, P. 2012, PhRvL, 108, 045001
Stansby, D., Horbury, T. S., & Matteini, L. 2019, MNRAS, 482, 1706
Stix, T. H. 1992, Waves in Plasmas (New York: AIP)
Sundkvist, D., Retinò, A., Vaivads, A., & Bale, S. D. 2007, PhRvL, 99, 025004
Taylor, G. I. 1938, RSPSA, 164, 476
Telloni, D., & Bruno, R. 2016, MNRAS Lett., 463, L79
Telloni, D., Bruno, R., & Trenchi, L. 2015, ApJ, 805, 46
Torrence, C., & Compo, G. P. 1998, BAMS, 79, 61
Tu, C. Y., & Marsch, E. 1995, SSRv, 73, 1
Vasquez, B. J. 2015, ApJ, 806, 33
Vasquez, B. J., Markovskii, S. A., & Smith, C. W. 2018, ApJ, 855, 121
Verscharen, D., Bourouaine, S., Chandran, B. D., & Maruca, B. A. 2013, ApJ, 773, 8
Verscharen, D., & Chandran, B. D. G. 2018, RNAAS, 2, 13
Verscharen, D., Klein, K. G., & Maruca, B. A. 2019, LRSP, 16, 5
Verscharen, D., & Marsch, E. 2011, AnGeo, 29, 909
Wicks, R. T., Alexander, R. L., Stevens, M. L., et al. 2016, ApJ, 819, 6
Wicks, R. T., Forman, M. A., Horbury, T. S., & Oughton, S. 2012, ApJ, 746, 103
Wicks, R. T., Horbury, T. S., Chen, C. H. K., & Schekochihin, A. A. 2010, MNRAS, 407, L31
Wilson, L. B., III, Stevens, M. L., Kasper, J. C., et al. 2018, ApJS, 236, 41
Woltjer, L. 1958a, PNAS, 44, 489
Woltjer, L. 1958b, PNAS, 44, 833
Woodham, L. D., Wicks, R. T., Verscharen, D., et al. 2019, ApJL, 884, L53
Woodham, L. D., Wicks, R. T., Verscharen, D., & Owen, C. J. 2018, ApJ, 856, 49
Yang, Y., Matthaeus, W. H., Parashar, T. N., et al. 2017, PhPl, 24, 072306
Zhao, G. Q., Feng, H. Q., Wu, D. J., et al. 2018, JGRA, 123, 1715
Zhao, G. Q., Feng, H. Q., Wu, D. J., et al. 2020a, ApJL, 889, L14
Zhao, G. Q., Feng, H. Q., Wu, D. J., Pi, G., & Huang, J. 2019a, ApJ, 871, 175
Zhao, G. Q., Li, H., Feng, H. Q., et al. 2019b, ApJ, 884, 60
Zhao, G. Q., Lin, Y., Wang, X. Y., et al. 2020b, GeoRL, 47, e2020GL089720
Zhao, G. Q., Lin, Y., Wang, X. Y., et al. 2021, ApJ, 906, 123